

# 1 Deciphering the role of evapotranspiration in declining relative humidity trends over land

2  
3 Yeonuk Kim,<sup>1\*</sup> Mark S. Johnson,<sup>1,2</sup>

## 4 5 **Affiliations**

6 <sup>1</sup> Institute for Resources, Environment and Sustainability, University of British Columbia,  
7 Vancouver, BC, Canada

8 <sup>2</sup> Department of Earth, Ocean and Atmospheric Sciences, University of British Columbia,  
9 Vancouver, BC, Canada

10 \* Correspondence to: Yeonuk Kim ([yeonuk.kim@ubc.ca](mailto:yeonuk.kim@ubc.ca))

## 11 **Abstract**

12 In recent decades, relative humidity over land ( $RH_L$ ) has declined, driving increases in droughts  
13 and wildfires. Previous explanations attribute this trend to insufficient moisture advection from  
14 the ocean to sustain  $RH_L$ , but this ignores atmospheric moisture supplied from terrestrial  
15 evapotranspiration ( $E_L$ ). Importantly, current state-of-the-art climate models underestimate the  
16 observed  $RH_L$  trend, and the cause is not fully understood. Here, we show that relative changes in  
17 humidity over land, unaccounted for by ocean advection, are quantitatively equivalent to relative  
18 changes in  $E_L$  on a global scale. This finding is consistent across climate models and climate  
19 reanalysis datasets, despite discrepancies in  $E_L$  trends among them. Differences in  $E_L$  trends are  
20 identified as the primary cause of the  $RH_L$  bias expressed in climate models. These results  
21 suggest that current climate models may overestimate  $E_L$  intensifications, leading to an  
22 underestimation of land-atmosphere drying, with significant implications for accurately  
23 predicting droughts, wildfires, and climate adaptation.

24  
25 **This manuscript is a non-peer reviewed preprint submitted to EarthArXiv.**

26 **INTRODUCTION**

27 Human-induced climate change is expected to have significant impacts on Earth's water cycle<sup>1</sup>.  
28 Reliable predictions of future water resources require a comprehensive understanding of how  
29 climate change affects land evapotranspiration ( $E_L$ )<sup>2-4</sup>, which represents the sum of evaporation  
30 from soil, intercepted water, and plant transpiration. While many studies have investigated the  
31 effects of climate change on actual  $E_L$ , the complex interactions between the atmosphere, land  
32 surface, soil moisture, and vegetation make it challenging to accurately predict changes in  $E_L$ .  
33 There are few long-term observational records of  $E_L$ , forcing a reliance on indirect methods to  
34 determine  $E_L$  trends at global and decadal scales. Our understanding of changes in  $E_L$  remains  
35 limited, exemplified by a substantial uncertainty in its estimated long-term changes<sup>5,6</sup> and a  
36 prolonged scientific debate about the impact of warmer and drier atmospheric conditions on  
37 future changes in  $E_L$ <sup>7-14</sup>.

38 The complexity of discerning the influence of anthropogenic climate change on  $E_L$  is further  
39 complicated by the reciprocal relationship between  $E_L$  and the atmospheric state. Atmospheric  
40 conditions not only serve as drivers of  $E_L$  but also are influenced by  $E_L$ , given that  $E_L$  acts as a  
41 significant moisture source to the air, particularly in inland regions<sup>15-20</sup>. Consequently, the  
42 uncertainty in  $E_L$  predictions has been identified as a significant contributor to uncertainty in  
43 atmospheric state predictions<sup>21,22</sup>. Paradoxically, however, the impacts of  $E_L$  on the near-surface  
44 atmosphere are frequently overlooked under the prevailing assumption that the atmospheric state  
45 acts primarily as a demand-side driver of  $E_L$ <sup>8</sup>.

46 Near-surface atmospheric observations in recent decades demonstrate an emergent decline in  
47 relative humidity over land ( $RH_L$ )<sup>23,24</sup>. This decline in observed  $RH_L$  is commonly explained  
48 using an ocean-influence theory<sup>25-27</sup>. This theory suggests that the amplified land warming  
49 compared to ocean warming is the primary cause of the  $RH_L$  decline since moisture advection  
50 from the ocean to the land is insufficient to maintain  $RH_L$  relative to increasing land surface  
51 temperatures. Consequently, warmer and drier atmospheric conditions over land are widely  
52 considered to drive a rapid increase in the atmospheric evaporative demand that could intensify  
53  $E_L$ <sup>7</sup>. However, this perspective ignores the reciprocal influences of  $E_L$  and the atmospheric  
54 state<sup>28-30</sup>. For example, recent studies suggest that soil moisture constrains moisture supplied to  
55 the air through  $E_L$ , and this  $E$ -influenced process is crucial to represent changes in  $RH_L$  over land  
56 in climate simulations<sup>31,32</sup>.

57 Therefore, it is essential to theoretically harmonize the influences on the atmospheric moisture  
58 budget over land resulting from (i)  $E_L$  and (ii) advected moisture from the ocean. This is  
59 particularly important as state-of-the-art climate models currently underestimate the well-  
60 established  $RH_L$  decline trend<sup>33-35</sup>. However, the fundamental reason for this bias remains  
61 unclear<sup>36</sup>. More importantly, this  $RH_L$  bias in climate models implies an underestimation of  
62 future drying and warming trends in model projections<sup>37</sup>. Therefore, a nuanced understanding of  
63 the influences of  $E_L$  on near-surface humidity trends over land is essential for accurately  
64 projecting future atmospheric conditions, water availability, and impacts of anthropogenic  
65 climate change on future droughts and wildfires.

66 Here, we aim to harmonize the influence of terrestrial  $E_L$  with the ocean-influence theory to more  
67 completely represent  $RH_L$  within an analytical framework. To this end, we first introduce a

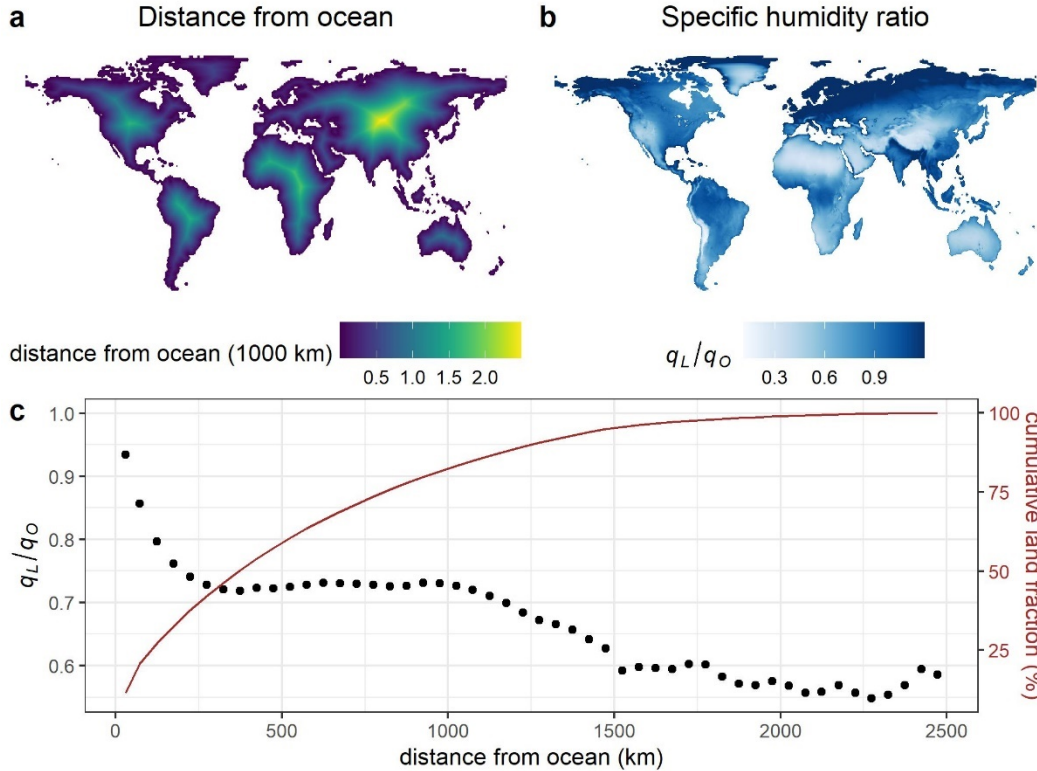
68 simple analytical equation explaining the relationship between changes in specific humidity and  
69  $E_L$  from a parsimonious boundary layer moisture budget, and evaluate the proposed equation  
70 using in-situ  $E_L$  observations from the FLUXNET2015 dataset<sup>38</sup>. We then integrate this equation  
71 representing the emerging  $E$ -influence theory with the ocean-influence theory. Using the ERA5<sup>39</sup>  
72 and JRA-3Q<sup>40</sup> reanalysis datasets and 27 general circulation models (GCMs) contained in the  
73 Coupled Model Intercomparison Project Phase 6 (CMIP6)<sup>41</sup>, we evaluate this integrated  
74 framework. In this way, we are able to analyze the physical constraints of changes in  $E_L$  and  
75 explain why CMIP6 climate models underestimate the emergent  $RH_L$  decline present in  
76 observations and reanalysis datasets.

## 77 **RESULTS**

### 78 ***E*-influence theory**

79 We begin by empirically assessing divergent theories regarding water vapor sources over land.  
80 On the one hand, it has been widely hypothesized that horizontal advection from the ocean is the  
81 primary source of water vapor over land<sup>7</sup>, forming the theoretical foundation of the ocean-  
82 influence theory<sup>25,26</sup>. However, other studies emphasize a dominant role for  $E_L$  as a moisture  
83 source to the air, especially for inland regions<sup>16,42,43</sup>.

84 We explore these conflicting hypotheses by examining the spatial variability of specific humidity  
85 ( $q$ ,  $\text{kg kg}^{-1}$ ) as a function of distance from the ocean (Fig. 1). On average, the ratio of specific  
86 humidity over land ( $q_L$ ) to specific humidity over the ocean ( $q_O$ ) decreases rapidly from the coast  
87 to  $\sim 250$  km inland, stabilizing thereafter for areas further inland. This finding that  $q_L$  is closer to  
88  $q_O$  for areas closer to the coast suggests that horizontal advection from the ocean may be a  
89 significant source of water vapor for areas located up to 250 km inland (constituting  
90 approximately 40% of the total land area, Fig. 1). However, horizontal advection of  $q_O$  appears to  
91 become relatively negligible for areas located further inland (i.e.,  $> 250$  km), where small  
92 horizontal gradients in  $q_L/q_O$  suggest that specific humidity in inland regions could be more  
93 significantly influenced by  $E_L$ . In fact, we find that  $q_L/q_O$  is nearly constant (i.e.,  $\frac{d}{dx}(\frac{q_L}{q_O}) \approx 0$ ) for  
94 areas located between 250 km and 1000 km from a coast, which represents another 40% of the  
95 total land area. Further declines in  $q_L/q_O$  for areas  $> 1000$  km inland imply increasing moisture  
96 limitations typical of arid regions.



97

98 **Fig. 1. Mean specific humidity ratio between land and ocean plotted against the distance**  
 99 **from ocean.** (a) Global map indicating the distance from ocean. (b) Global map of the mean  
 100 specific humidity ratio between land ( $q_L$ ) and ocean ( $q_O$ ) in the ERA5 reanalysis over the period  
 101 1973-2022. The time-averaged  $q_L$  is calculated for each grid, while the time-averaged  $q_O$  is  
 102 determined as the zonal mean at that latitude to represent the neighboring ocean. (c) Relationship  
 103 between  $q_L/q_O$  and the distance from ocean. The black dot represents the mean  $q_L/q_O$ , calculated  
 104 for binned distances from the ocean (each bin has 50 km). The cumulative land fraction (brown  
 105 line) is included as a reference.  
 106

107 The empirical, emergent characteristics of  $\frac{d}{dx} \left( \frac{q_L}{q_O} \right)$  in Fig. 1 prompts a reexamination of the  
 108 derivation of the ocean-influence theory, given that horizontal advection (driven by horizontal  $q$   
 109 gradients) doesn't always emerge as the predominant moisture source, particularly over inland  
 110 regions. Byrne and O’Gorman<sup>26</sup> proposed a parsimonious steady-state moisture budget for a  
 111 boundary layer box over land (Fig. S1), which assumes negligible  $E_L$  in order to derive a simple  
 112 moisture constraint, as expressed by Eq. 1:

113 
$$\frac{\Delta q_L}{q_L} = \frac{\Delta q_O}{q_O} \tag{1}$$

114 where  $\Delta$  indicates the temporal change between two periods. Eq. 1 is a summary of the ocean-  
 115 influence theory, which was introduced to explain the observed decline in  $RH_L$  using the ocean  
 116 advection<sup>25-27</sup>. The derivation of Eq. 1 involved assumptions of constant values for horizontal

117 and vertical mixing velocities, boundary layer heights, and the specific humidity jump rate at the  
118 top of the boundary layer.

119 To maintain compatibility with this theoretical framework, we adopt the same moisture budget  
120 equation and assumptions for Eq. 1 while considering horizontal advection as negligible,  
121 focusing instead on the influence of  $E_L$ . In this scenario, the changes in specific humidity over  
122 land can be expressed as follows (for detailed derivation, refer to Methods):

$$123 \quad \frac{\Delta q_L}{q_L} = \frac{\Delta E_L}{E_L} \quad (2)$$

124 Eq. 2 is the proposed theoretical constraint for changes in  $q_L$  and  $E_L$  when horizontal moisture  
125 advection is negligible and thus  $q_L$  is predominantly controlled by  $E_L$ . By rearranging Eq. 2 for  
126  $\Delta E_L$  and partitioning  $\Delta q_L$  into relative humidity and temperature components, we can write as  
127 follows.

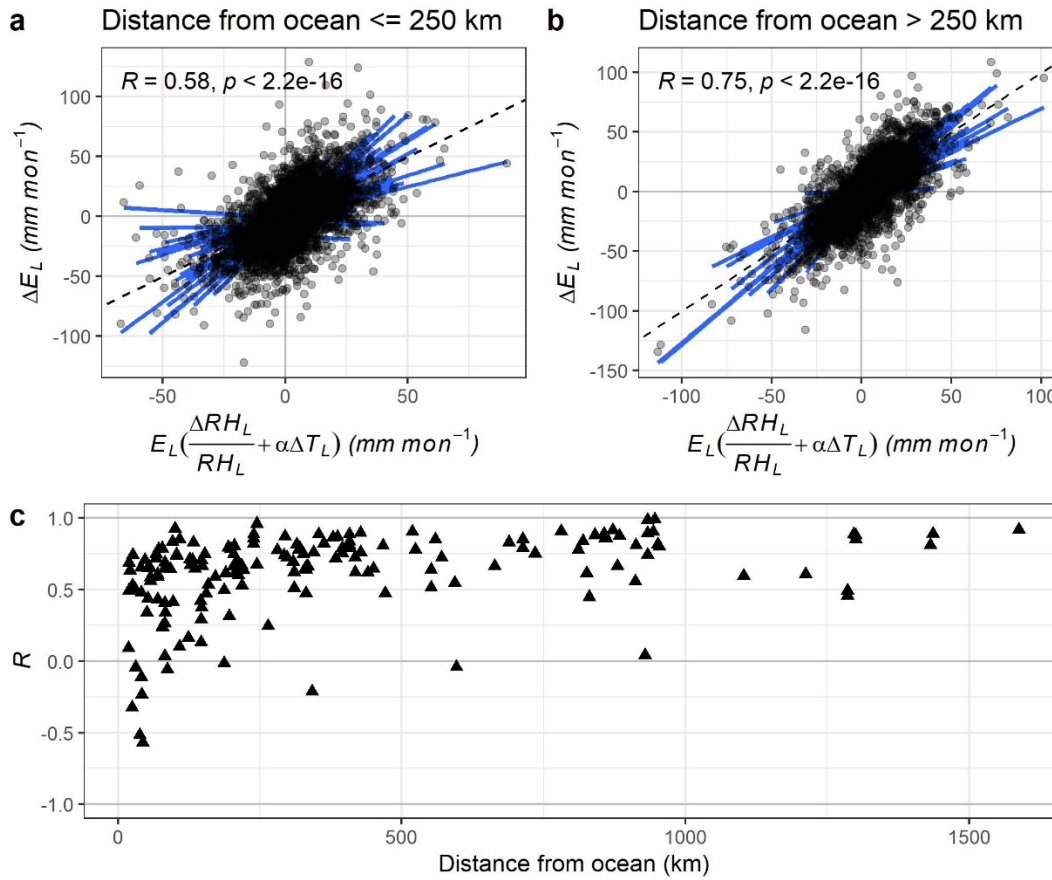
$$128 \quad \Delta E_L = E_L \frac{\Delta q_L}{q_L} \\ 129 \quad = E_L \left( \frac{\Delta RH_L}{RH_L} + \alpha \Delta T_L \right) \quad (3)$$

130 where  $RH_L (= \frac{q_L}{q^*(T_L)})$  is the near-surface relative humidity over land,  $q^*(T_L)$  is saturation specific  
131 humidity at the near-surface air temperature ( $T_L$ ),  $\alpha (= \frac{s}{q^*(T)})$  is the sensitivity of saturation  
132 specific humidity to temperature, and  $s (= \frac{dq^*}{dT})$  is the linearized saturation specific humidity  
133 slope versus temperature. Here, we approximate relative humidity using specific humidity  
134 instead of water vapor pressure and linearize the Clausius-Clapeyron relationship.

135 Eq. 3 implies that one can simply determine  $\Delta E_L$  only using atmospheric observations. However,  
136 while Eq. 1 has undergone evaluation in several prior studies<sup>25-27,44</sup>, the viability of the proposed  
137 Eq. 3 demands a comprehensive assessment. Evaluating the proposed theory represented by Eq.  
138 3 presents a challenge due to the absence of reliable long-term  $\Delta E_L$  observations, particularly at  
139 global scale, given that  $E_L$  is more challenging to observe than specific humidity.

140 Alternatively, we assessed the feasibility of Eq. 3 using observed seasonal changes in  $\Delta E_L$  at the  
141 field scale (e.g., up to a few square kilometers). We used FLUXNET2015 monthly-scale  $E_L$  and  
142 meteorological observations from 170 sites worldwide<sup>38</sup>. We estimated  $\Delta E_L$  from Eq. 3 using  
143 monthly differences in  $RH_L$  and  $T_L$ . Subsequently, we compared observed values for  $\Delta E_L$  with  
144 those estimated for  $\Delta E_L$  using Eq. 3. We find that Eq. 3 effectively estimates the observed  $\Delta E_L$ ,  
145 particularly in inland regions (Fig. 2). The majority of inland sites ( $> 250$  km from the ocean)  
146 exhibit a high correlation coefficient ( $R$ ) between observed  $\Delta E_L$  and its estimation using Eq. 3,  
147 with regression slopes close to one. On the other hand, the correlation between  $\Delta E_L$  and its  
148 estimation from Eq. 3 is lower for several sites located closer to a coast ( $\leq 250$  km from ocean).  
149 These field-scale results support the viability of Eq. 3, especially in inland regions where  
150 horizontal moisture advection from the ocean becomes increasingly negligible for increasing

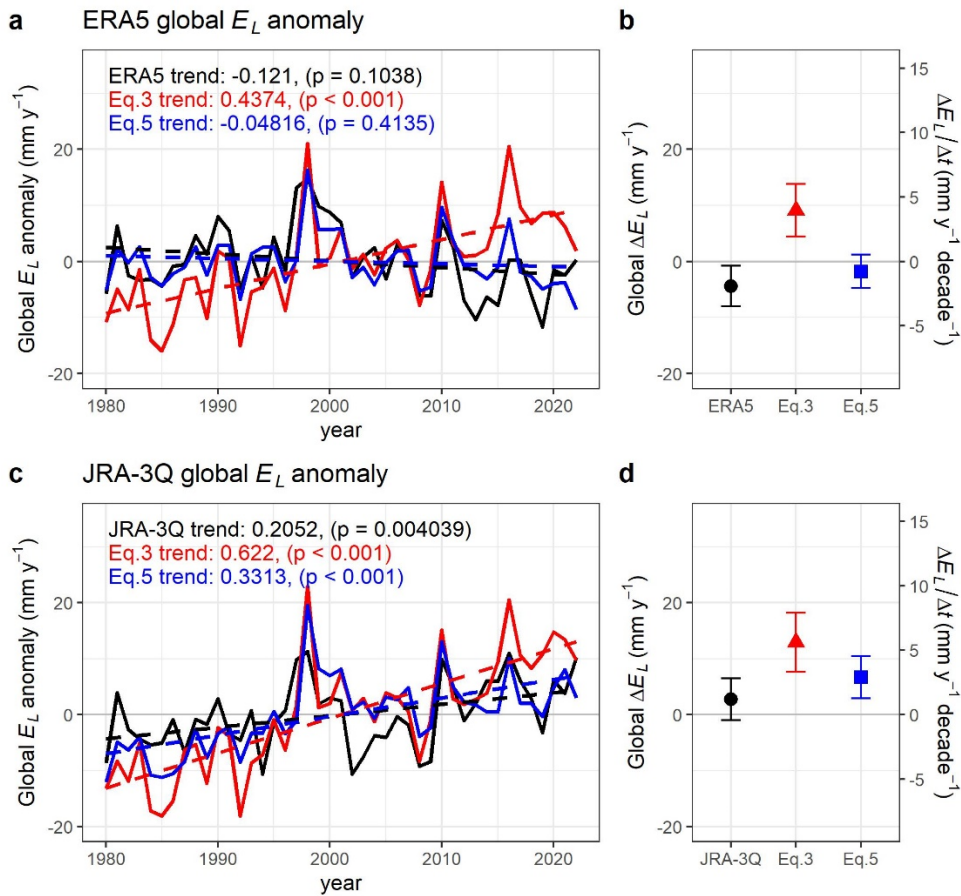
151 distance from the coast. It is worth noting that the robustness of this result persisted when  
 152 substituting the  $E_L$  observations with the energy balance-corrected version of  $E_L$  (see Fig. S2).



153  
 154 **Fig. 2. Evaluation of Eq. 3 at regional scale using FLUXNET2015 dataset.** Scatter plot  
 155 depicting  $\Delta E_L$  and its estimation using Eq. 3 for (a) pericoastal sites (distance from the ocean  $\leq$   
 156 250 km) and (b) inland sites (distance from the ocean  $>$  250 km). Blue lines represent linear  
 157 regression lines for each site, and black dashed lines indicate one-on-one lines. (c) Correlation  
 158 ( $R$ ) between  $\Delta E_L$  and  $E_L \left( \frac{\Delta RH_L}{RH_L} + \alpha \Delta T_L \right)$  for each site (y-axis) versus the distance from the ocean  
 159 for each site (x-axis).  
 160

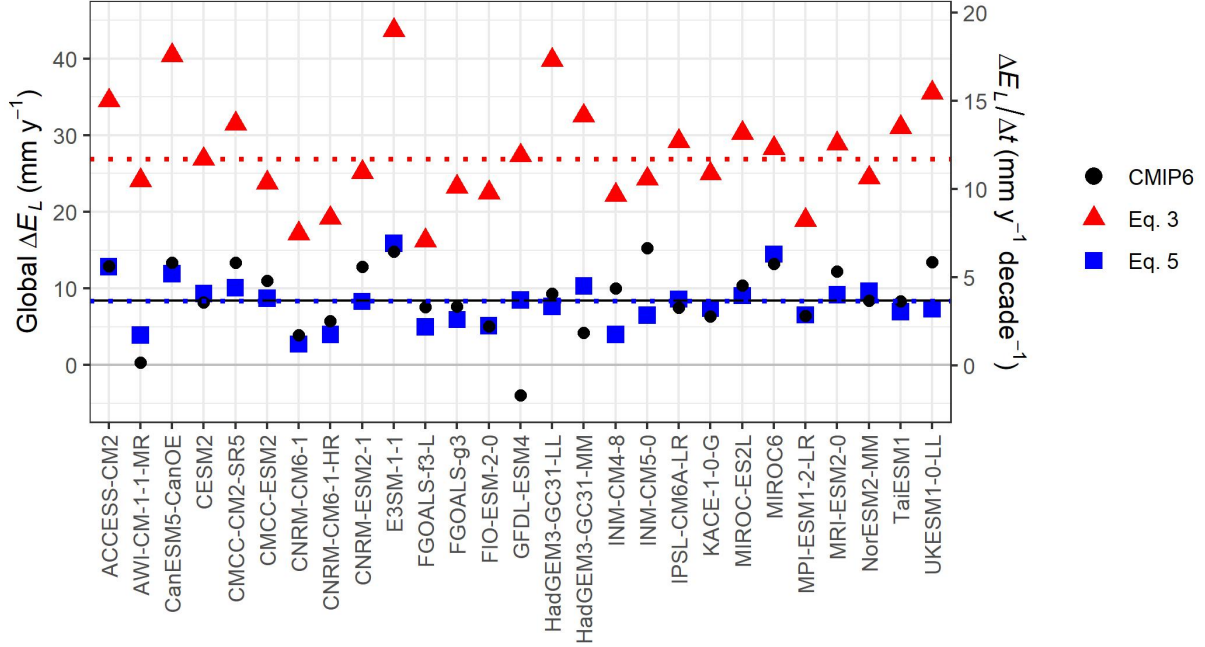
161 While the evaluation at field and seasonal scales supports Eq. 3, it is important to note that the  
 162 direct applicability of Eq. 3 for inferring long-term changes in global  $E_L$  remains to be  
 163 established. We also note that the omission of horizontal advection from the ocean in the  
 164 derivation of Eq. 3 is unrealistic on a global scale, necessitating an additional line of inquiry. To  
 165 further assess the performance of Eq. 3 at the global level, we employed modeled  $\Delta E_L$  and  
 166 atmospheric state from two latest generation reanalysis datasets and from climate simulations,  
 167 assuming that  $\Delta E_L$  and atmospheric state in each climate model represent internally consistent  
 168 representations of the land-atmosphere-ocean coupled system<sup>14</sup>. Specifically, we focus on non-  
 169 Polar regions located 66.5°S to 66.5°N in order to exclude the Arctic and Antarctica since the  
 170 ocean-influence theory is better justified at lower latitudes<sup>27</sup>.

171 Our analysis revealed that Eq. 3 consistently overestimates global land  $\Delta E_L$  for the recent 43  
 172 years (1980-2022) in ERA5 and JRA-3Q reanalysis datasets (Fig. 3), as well as for all 27 GCMs  
 173 in CMIP6 (Fig. 4). This suggests a systematic bias in Eq. 3 on the global scale, despite its  
 174 reasonable performance at regional and seasonal scales. At the regional scale, horizontal  
 175 moisture advection can be both positive and negative, depending on the dryness of nearby  
 176 regions, but horizontal advection from ocean to land is always positive at the global scale as  $q_O$   
 177 is always greater than  $q_L$ . Therefore,  $\Delta q_L$  not only increases due to the rise in  $E_L$ , but also increases  
 178 due to heightened ocean advection that is driven by the increasing  $q_O$  in a warming climate.  
 179 Consequently, the simplifying assumptions of Eq. 3 lead to overestimation of global-scale  
 180 changes in  $E_L$ , suggesting that an additional term is needed to represent the influence of ocean  
 181 advection. We now turn our attention to incorporating ocean advection into Eq. 3.



182  
 183 **Fig. 3. Evaluation of Eq. 3 and Eq. 5 at global scale relative to ERA5 and JRA-3Q**  
 184 **reanalysis datasets.** (a) Global land  $E_L$  anomaly from ERA5 reanalysis (black), Eq. 3 (red), and  
 185 Eq. 5 (blue) over the period 1980-2022. Dashed lines represent linear trends. (b) Global  $\Delta E_L$   
 186 from ERA5 reanalysis (black), Eq. 3 (red), and Eq. 5 (blue), calculated as the difference between  
 187 current (2003-2022) and past climate (1980-1999). Error bars represent the 95% confidence  
 188 intervals, and the secondary y-axis shows the average rate of change. (c) Similar to panel (a) but  
 189 using JRA-3Q reanalysis. (d) Similar to panel (b) but using JRA-3Q reanalysis. In this figure,  
 190 Eqs. 3 and 5 are calculated using atmospheric variable from each reanalysis, and the artic  
 191 ( $>66.5^\circ\text{N}$ ) and antarctica ( $<66.5^\circ\text{S}$ ) are masked.

192



193 **Fig. 4. Evaluation of Eq. 3 and Eq. 5 at global scale using CMIP6 climate models.** Global  
 194  $\Delta E_L$  from each climate model (black), Eq. 3 (red), and Eq. 5 (blue), calculated as the difference  
 195 between current (2003-2022) and past climate (1980-1999). Dotted lines indicate median of Eq.  
 196 3 (red) and Eq. 5 (blue) while the black solid line indicates median of CMIP6. In this figure,  
 197 polar regions ( $>66.5^\circ\text{N}$  and  $<66.5^\circ\text{S}$ ) are masked.  
 198  
 199

## 200 Reintroducing ocean advection

201 Our analysis, illustrated in Figs. 3 and 4, indicates that Eq. 3 consistently overestimates long-  
 202 term changes in  $E_L$  on a global scale, across all examined climate models and reanalysis datasets.  
 203 We propose that this overestimation may be attributed to the horizontal advection of moisture  
 204 from the ocean, considering that a portion of the change in  $q_L$  can be attributable to  $\Delta E_L$ , while  
 205 another portion results from oceanic advection. To account for the impact of ocean advection  
 206 within this simple scaling framework, we account for the component of  $\Delta q_L$  that can be attributed  
 207 to ocean advection. This adjustment is based on the ocean-influence theory (i.e., Eq. 1), as  
 208 follows:

$$\begin{aligned}
 209 \quad \Delta E_L &= E_L \left( \frac{\Delta q_L}{q_L} - \gamma \frac{\Delta q_O}{q_O} \right) \\
 210 \quad &\approx E_L \left( \frac{\Delta RH_L}{RH_L} + \alpha \Delta T_L - \gamma \alpha \Delta T_O \right) \quad (4)
 \end{aligned}$$

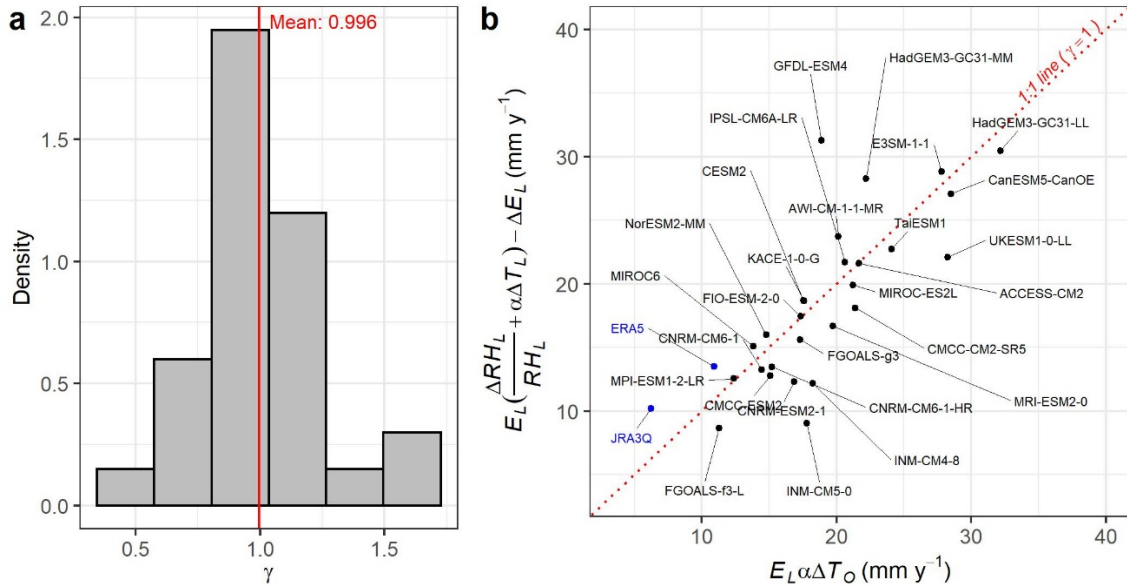
211 where  $\gamma$  is a parameter introduced in our study to refine the ocean-influence theory, and  $T_O$   
 212 is near-surface air temperature over the ocean. Here, we decompose  $\Delta q$  into relative humidity and  
 213 temperature components similar to Eq. 3 by assuming a time-constant  $RH$  over ocean<sup>45,46</sup>.



214 In this simple scaling, the ocean advection is embedded in the last term of the right-hand side of  
 215 Eq. 4. The introduction of  $\gamma$  aims to account for potential discrepancies that might arise when Eq.  
 216 1 is applied to scenarios where moisture from  $E_L$  significantly contributes to  $\Delta q_L$ , an aspect not  
 217 explicitly covered in the original derivation of the ocean-influence theory. If Eq. 1, even within  
 218 our theoretical framework, accurately depicts the ocean advection impact, then  $\gamma$  will be set to  
 219 unity. Using CMIP6 GCMs along with ERA5 and JRA-3Q reanalysis data, we have determined  
 220 that  $\gamma$  approximates unity on a global scale (Fig. 5), reinforcing the applicability of the ocean-  
 221 influence theory within our scaling. Consequently, we adopt  $\gamma$  as unity, leading to the following  
 222 refined equation:

$$223 \quad \Delta E_L \approx E_L \left( \frac{\Delta RH_L}{RH_L} + \alpha \Delta T_L - \alpha \Delta T_O \right) \quad (5)$$

224 Equation 5 serves as our proposed model to estimate the long-term trend of  $E_L$  on a global scale  
 225 using atmospheric variables and accounting for ocean advection. Consistent with the previous  
 226 section, we apply Eq. 5 to ERA5 and JRA-3Q reanalysis data and CMIP6 GCMs. Our results  
 227 show that Eq. 5 effectively reproduces the direct  $\Delta E_L$  output from reanalysis (Fig. 3).  
 228 Furthermore, not only does it capture the long-term  $\Delta E_L$ , but Eq. 5 also reasonably replicates the  
 229 interannual variability of global land  $E_L$ , particularly in the ERA5 climate reanalysis dataset  
 230 ( $R=0.69$ ). Also,  $\Delta E_L$  estimations using Eq. 5 exhibit a much closer match with the direct  $\Delta E_L$   
 231 output from CMIP6 GCMs compared to Eq. 3 (Fig. 4).



232 **Fig. 5. Evaluation of Parameter  $\gamma$ .** Panel (a) displays a histogram with the mean value of  $\gamma$  from  
 233 CMIP6 GCMs and ERA5, JRA-3Q reanalysis datasets. Panel (b) offers a one-to-one plot  
 234 between  $E_L \left( \frac{\Delta RH_L}{RH_L} + \alpha \Delta T_L \right) - \Delta E_L$  and  $E_L \alpha \Delta T_O$  for individual CMIP6 models (black dots) and  
 235 reanalysis datasets (blue dots). Alignment with the one-to-one line indicates  $\gamma$ 's approximation to  
 236 unity, validating our approach to adopt  $\gamma$  as unity for simplifying the scaling equation. In this  
 237 figure, polar regions ( $>66.5^\circ N$  and  $<66.5^\circ S$ ) are masked to determine  $\gamma$  since the ocean-influence  
 238 theory is better justified at lower latitudes<sup>27</sup>.

240

241 **Why do CMIP6 models underestimate the observed decline in  $RH_L$ ?**

242 To gain a deeper insight into the drivers behind  $RH_L$  decline in recent decades, we reorganize the  
 243 proposed theory (Eq. 5) and the ocean-influence theory (Eq. 1) as follows:

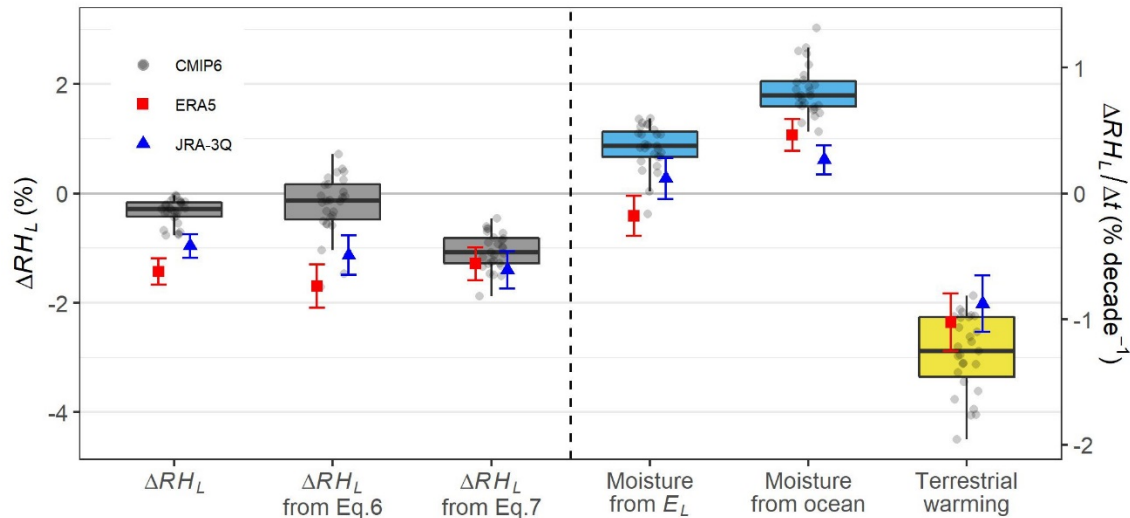
$$244 \quad \Delta RH_L = RH_L \left( \overbrace{\frac{\Delta E_L}{E_L}}^{\text{water vapor supply}} + \underbrace{\alpha \Delta T_O}_{\text{from ocean}} - \overbrace{\alpha \Delta T_L}^{\text{warming}} \right) \quad (6)$$

$$245 \quad \Delta RH_L = RH_L \left( \underbrace{\alpha \Delta T_O}_{\text{from ocean}} - \overbrace{\alpha \Delta T_L}^{\text{warming}} \right) \quad (7)$$

246 Eq. 6 describes changes in  $RH_L$  according to the proposed theory, while Eq. 7 describes changes  
 247 in  $RH_L$  according to the ocean-influence theory. The sole disparity between the two equations  
 248 lies in the initial term of Eq. 6, which represents the water vapor supply from  $E_L$ .  $RH_L$  can  
 249 decline if the increase in water vapor supply is slower than the increase in saturation vapour  
 250 pressure resulting from atmospheric warming. On the other hand,  $RH_L$  may remain steady if the  
 251 water vapor supply is sufficiently large to offset the warming effect of increasing atmospheric  
 252 moisture storage capacity due to the Clausius-Clapeyron relation. Therefore, decomposing  $\Delta RH_L$   
 253 into three components using Eq. 6 can help identify the primary sources of the difference  
 254 between reanalysis and CMIP6 climate models.

255 Fig. 6 presents the results of applying Eqs. 6 and 7 to the two reanalysis datasets and CMIP6  
 256 GCMs. The first column shows that the decline in  $RH_L$  is underestimated in CMIP6 models  
 257 compared to ERA5 and JRA-3Q. The second column demonstrates that Eq. 6 can reasonably  
 258 replicate this difference in terms of the ensemble median  $\Delta RH_L$ , although CMIP6 models exhibit  
 259 more variability. If we omit the first term of Eq. 6 as implied in Eq. 7,  $\Delta RH_L$  from CMIP6 aligns  
 260 closely with reanalysis (third column of Fig. 6). This result suggests that the difference in  $\Delta E_L$   
 261 between CMIP6 and reanalysis is a significant contributor to the  $\Delta RH_L$  bias.

262 Specifically, we found that the difference in water vapor supply from  $E_L$  between reanalysis and  
 263 CMIP6 is sufficient to account for the difference in  $\Delta RH_L$  between the two. The ocean advection  
 264 term is also higher in CMIP6 than in reanalysis, but this effect roughly cancels out as terrestrial  
 265 warming is also higher in CMIP6 than in reanalysis. This implies that the larger ocean warming  
 266 in CMIP6 compared to observations in the recent decade cannot entirely explain the  $\Delta RH_L$  bias  
 267 in CMIP6 because the amplified terrestrial warming is also higher in CMIP6. This result aligns  
 268 with recent studies<sup>35,47</sup>, which demonstrated that climate models prescribing observed ocean  
 269 warming cannot completely resolve the  $\Delta RH_L$  bias issue.



270  
 271 **Fig. 6. Attribution of  $\Delta RH_L$  based on Eq. 6.** Box plots with jitter points depict CMIP6 models,  
 272 while the red squares with error bars represent ERA5, and the blue triangles with error bars  
 273 represent JRA-3Q. The first column is  $\Delta RH_L$ , the second column is the estimated  $\Delta RH_L$  using Eq.  
 274 6, and the third column is the estimated  $\Delta RH_L$  using Eq. 7. The last three columns provide a  
 275 breakdown of each term in Eq. 6. Here  $\Delta$  indicates difference between current (2003-2022) and  
 276 past climate (1980-1999). Error bars represent the 95% confidence intervals, and the secondary  
 277 y-axis shows the average rate of change.  
 278

## 279 DISCUSSION

### 280 Overestimated $E_L$ intensification in climate models

281 Our analysis illustrated in Fig. 6 suggests a potential overestimation of the intensification of  
 282 terrestrial  $E_L$  in climate simulations, leading to a bias in  $\Delta RH_L$ . This interpretation aligns with  
 283 findings from a recent study<sup>37</sup>, which identified certain plausible climate models within CMIP6  
 284 that exhibit a drier  $\Delta RH_L$ . Notably, these plausible models generally demonstrate a weaker  
 285 increase in  $E_L$  compared to other models, supporting our interpretation. If the intensification of  
 286  $E_L$  is indeed exaggerated in current state-of-the-art climate models, and if future projections also  
 287 suffer from the same issue, as indicated by Douville and Willett<sup>37</sup>, several significant  
 288 implications may arise.

289 Firstly, the anticipated reduction in future soil moisture could be more severe than currently  
 290 predicted by most models included in CMIP6. This is consequential because soil moisture  
 291 reduction serves as a primary driver of the limited increase in  $E_L$ , leading to a decline in  $RH_L$  in  
 292 climate models<sup>31,32</sup>. Secondly, the future ratio between annual mean runoff and annual mean  
 293 precipitation (i.e., runoff ratio) might be underestimated due to the overestimated  $E_L$ <sup>37</sup>. The  
 294 underestimated runoff ratio could imply a miscalculation of extreme flood events in the future  
 295 based on current climate model projections. Thirdly, in alignment with the concerns raised by a  
 296 recent study<sup>35</sup>, the danger of wildfires and heatwaves may be more severe than predicted based  
 297 on current climate models. If future  $E_L$  is constrained ( $\Delta E_L \approx 0$ ), while  $RH_L$  decreases and

298 temperature increases, extremely dry and hot weather conditions could become even more  
299 severe<sup>48</sup>. These implications highlight the importance of accurately modeling terrestrial  
300 evapotranspiration for a comprehensive understanding of future climate-related risks.

### 301 **Reconciling with the ocean-influence theory**

302 Byrne and O’Gorman<sup>27</sup> demonstrated that a simple ocean advection constraint, as summarized  
303 in Eq. 1, along with another constraint on moist static enthalpy, can explain the observed decline  
304 in  $RH_L$  over land. At first glance, this ocean-influence theory may seem to be in contradiction  
305 with our proposed theoretical framework. However, reconciliation between the two theoretical  
306 frameworks is possible if  $\Delta E_L$  is close to zero in Eq. 5.

307 Indeed, our analysis reveals that there are no significant global land  $E_L$  trends in ERA5 and JRA-  
308 3Q reanalysis for the past 43 years, although ERA5 suggests a slightly negative trend and JRA-  
309 3Q suggests a slightly positive trend (Fig. 3). These subtle global land  $E_L$  trends in reanalyses do  
310 not lead to significant differences in  $\Delta RH_L$  estimation between the ocean-influence theory and  
311 our proposed theoretical framework (Fig. 6, third and second columns). These results suggest  
312 that the conventional ocean-influence theory and the present work can both be compatible within  
313 ERA5 and JRA-3Q, which is known to assimilate in situ humidity observations and thus  
314 accurately reproduce the observed declining trend of  $RH_L$ <sup>34,35</sup>.

315 On the other hand, most CMIP6 GCMs estimate positive global land  $E_L$  trends for the past 43  
316 years (Fig. 4). This is equivalent to  $\frac{\Delta q_L}{q_L} > \frac{\Delta q_O}{q_O}$  in our theoretical framework. In other words, if an  
317 increase in  $q_L$  is faster than the rate suggested by the ocean-influence theory, it could imply an  
318 intensification of global land  $E_L$ . Recently, Seltzer, et al.<sup>44</sup> found that the paleotemperature  
319 proxies suggested  $\Delta q_L = 0.84\Delta q_O$ , where 0.84 is approximately 10-20% larger than recent  
320 observations of  $\frac{q_L}{q_O}$  (= 0.72) at the global scale<sup>27</sup>. This suggests that changes in  $q_L$  are faster than  
321 the rate suggested by the ocean-influence theory at the last glacial maximum, and it could  
322 potentially signify changes in  $E_L$  within the context of Eq. 5. Consequently, our theoretical  
323 framework remains consistent with recent paleotemperature proxies as well.

### 324 **Theoretical upper limit of increases in global $E_L$**

325 Although our initial, simplified  $E$ -influence theory in Eq. 3, which ignores ocean advection,  
326 tends to overestimate the global trend of  $E_L$  (Figs. 3 and 4), it provides a clear upper limit for the  
327 increase in global  $E_L$  based on the observed humidity trend over land. Specifically, considering  
328 that the ERA5 and JRA-3Q reanalysis closely aligns with the current trend of  $RH$  observations  
329 compared to climate simulations, Eq. 3 calculated using reanalysis meteorological data in Fig. 3  
330 (i.e.,  $4 \sim 6 \text{ mm y}^{-1} \text{ decade}^{-1}$ ) could serve as an upper limit for the increase in global  $E_L$  over past  
331 decades. It is unlikely for the global  $E_L$  increase to surpass this limit unless specific humidity  
332 over the ocean decreases, a scenario deemed unrealistic under a warming climate<sup>49,50</sup>.

333 This upper limit based on humidity observations holds significance due to the substantial  
334 uncertainty in estimating the long-term global trend of  $E_L$ <sup>5,6</sup>. While recent water balance  $E_L$   
335 estimations suggest a slight decreasing  $E_L$  trend<sup>51</sup>, numerous remote sensing-based  $E_L$  estimates,

336 employing physical equations, exceed  $4 \sim 6 \text{ mm y}^{-1} \text{ decade}^{-1}$ <sup>5,6</sup>. Physically based  $E_L$  estimates  
337 from remote sensing often heavily depend on increases in temperature and net radiation, with the  
338 decrease in  $RH_L$  rarely considered or treated as an increase in  $E_L$  based on the atmospheric  
339 evaporative demand concept. However, our theory and analysis consistently demonstrate that a  
340 decrease in  $RH_L$  over this decadal time scale should not be interpreted as an increase in  $E_L$ .  
341 Rather, the decrease in  $RH_L$  should be understood as a consequence of a smaller increase in  $E_L$  to  
342 the water vapour supply within a coupled atmospheric boundary layer. This discrepancy in  
343 perspective may contribute to biases in physically based  $E_L$  estimations.

#### 344 **Potential caveats and outlook**

345 In this study, we present simple theoretical frameworks based on meteorological information to  
346 elucidate the source variability in  $E_L$  for climate models vs. observational data and reanalysis  
347 products. We employed this approach to evaluate trends in atmospheric humidity and  $E_L$  over  
348 past decades, particularly on a global scale. While our theory aligns consistently with  
349 observations, reanalysis, and climate models, certain limitations should be acknowledged in our  
350 methodology.

351 Firstly, our simple physical model relies on several simplified assumptions. For instance, Eq. 3  
352 neglects local horizontal moisture advection, which could be a significant factor. Although Eq. 5  
353 is introduced to account for horizontal moisture advection, it is only plausible at a global spatial  
354 scale, and therefore, it cannot accurately represent horizontal moisture advection at local scale.  
355 Consequently, our approach is not suitable for assessing regional scale long-term changes in  $E_L$ .  
356 A future study could enhance the model's regional scale applicability by incorporating additional  
357 advection terms into Eq. 5 or 3, providing a more accurate representation of local advection  
358 processes to understand regional changes in  $E_L$ .

359 Secondly, our approach is an analytical model instead of a process-based model, and as such, it  
360 cannot explain why  $E_L$  remained steady in reanalysis and was overestimated in CMIP6 climate  
361 simulations. This discrepancy could be related to surface parameterizations, considering factors  
362 such as stomatal closure due to the  $\text{CO}_2$  fertilization effect<sup>47</sup>. Soil moisture limitation on  $E$  is  
363 another potential mechanism<sup>31,32</sup>. To better grasp the origin of this issue, future studies may  
364 explore the relationship between satellite soil moisture,  $E_L$ , and atmospheric humidity. Also, it is  
365 important to conduct experiments using land surface models with varying parameters or model  
366 structures to better understand the origin of the bias.

## 367 **Methods**

### 368 **FLUXNET2015 data**

369 To assess the proposed Eq. 3, we used the FLUXNET2015 Tier One (CC-BY-4.0) dataset<sup>38</sup>. This  
370 global dataset includes 212 in-situ eddy-covariance flux tower sites around globe representing  
371 over 1,500 site years. Monthly records of latent heat flux, air temperature, vapor pressure deficit,  
372 and air pressure were obtained from the FLUXNET data portal  
373 (<https://fluxnet.org/data/fluxnet2015-dataset/>). We only included data for periods for which the  
374 quality control flag indicated more than 80% of the half-hourly data were used for generating the  
375 monthly datasets (i.e., measured data or good quality gap-filled data). Also, we only included  
376 data points with positive latent heat flux. Additionally, we considered only sites with at least  
377 three consecutive months of available data. Following these filtering processes, 170 flux sites  
378 around the globe were retained.

379 The calculation of  $E_L$  was derived from latent heat flux,  $\alpha$  from temperature ( $\alpha = \frac{s}{q^*(T)} = \frac{L_v}{R_v T^2}$ ,  
380 where  $L_v$  is latent heat of vaporization and  $R_v$  is the gas constant for water vapor), and  $RH$  from  
381 temperature, air pressure, and vapor pressure deficit using the bigleaf R package<sup>52</sup>. The  
382 multiplications of  $\Delta RH_L$  and  $\Delta T_L$  in Eq. 3 were averaged values over the two months, with  $\Delta RH_L$   
383 and  $\Delta T_L$  calculated as the difference between the two months. In Fig. 2, observed latent heat flux,  
384 without energy balance correction, was employed. Notably, we found similar results when using  
385 the energy balance correction version of latent heat flux, incorporating the Bowen ratio  
386 preservation method<sup>38,53</sup> (see Fig. S2).

### 387 **ERA5 and JRA-3Q reanalysis**

388 To evaluate the proposed theoretical framework, we employed ERA5, the latest reanalysis  
389 product from the European Center for Medium Range Weather Forecasts (ECMWF)<sup>39</sup>, and JRA-  
390 3Q, the latest reanalysis product from the Japan Meteorological Agency<sup>40</sup>. It is worth noting that,  
391 in this study, we deliberately excluded MERRA2 reanalysis, another widely used reanalysis  
392 product by the National Aeronautics and Space Administration (NASA). This decision was  
393 based on MERRA2's limitation of not assimilating in situ humidity observations and its  
394 documented tendency to overestimate specific humidity trends<sup>35</sup>.

395 We obtained ERA5 single level (near-surface) output from the Climate Data Store (CDS) of  
396 ECMWF (<https://doi.org/10.24381/cds.f17050d7>), and JRA-3Q single level (near-surface: 2 m  
397 height) output at 1.25 degree spatial resolution from the Data Integration and Analysis System  
398 (DIAS) (<https://doi.org/10.20783/DIAS.645>). We obtained monthly records of latent heat flux,  
399 air pressure, air temperature, and dewpoint temperature for the period of 1980-2022. We then  
400 calculated  $E$  from latent heat flux,  $\alpha$  from temperature, and  $RH$  from temperature, air pressure,  
401 and dewpoint temperature using the bigleaf R package<sup>52</sup>.

### 402 **CMIP6 models**

403 In addition to the two reanalysis datasets, we incorporated data from 27 climate models within  
404 the CMIP6<sup>41</sup>. The complete list of the utilized climate models is detailed in Table S1. For the

405 analysis, we employed the Historical simulation covering the period from 1980 to 2014. Given  
 406 that the historical simulation ended in 2014, we augmented our dataset with Shared  
 407 Socioeconomic Pathway 5-8.5 (SSP5-8.5) simulations for the subsequent period from 2015 to  
 408 2022 to ensure comparability with the reanalysis datasets. We obtained monthly scale climate  
 409 models' output from CDS of ECMWF (<https://doi.org/10.24381/cds.c866074c>). Latent heat flux,  
 410 near-surface air temperature, near-surface air specific humidity, and surface air pressure were  
 411 retrieved. We then calculated  $E$  from latent heat flux,  $\alpha$  from temperature, and  $RH$  from  
 412 temperature, air pressure, and specific humidity.

### 413 Derivation of the $E$ -influence theory

414 Byrne and O’Gorman<sup>26</sup> introduced an idealized atmospheric boundary layer (ABL) box model  
 415 to elucidate the relationship among horizontal moisture advection from the ocean, terrestrial  $E_L$ ,  
 416 and the vertical relaxation flux of moisture at the top of the ABL (e.g., entrainment). This  
 417 idealized box model assumes a fixed ABL height and can be conceptualized as a diel-averaged  
 418 ABL, similar to another ABL box model introduced elsewhere<sup>16,18</sup>. The moisture budget within  
 419 the ABL box over land can be expressed as follows (Fig. S1):

$$420 \quad h_L \frac{dq_L}{dt} = \frac{h_O}{l} \rho v_1 (q_O - q_L) + \frac{h_L - h_O}{l} \rho v_1 (q_{FT,O} - q_L) + \rho v_2 (q_{FT,L} - q_L) + E_L \quad (8)$$

421 where  $h$  is the boundary layer height,  $l$  is the length of the land,  $q$  is specific humidity,  $v_1$  is  
 422 horizontal mixing velocity,  $v_2$  is vertical mixing velocity, and  $\rho$  is the air density. The subscripts  
 423  $O$  and  $L$  respectively denote ocean and land, while the subscript  $FT$  indicates the free troposphere  
 424 immediately above the land and ocean boundary layers. Under steady-state conditions, the right-  
 425 hand side is set to zero (i.e.,  $\frac{dq_L}{dt} = 0$ ). Byrne and O’Gorman<sup>26</sup> further simplified Eq. 8 by  
 426 assuming that the free-tropospheric specific humidity is directly proportional to the ABL specific  
 427 humidity, denoted as  $q_{FT,L} = \lambda_L q_L$  and  $q_{FT,O} = \lambda_O q_O$ , where  $\lambda_L$  and  $\lambda_O$  are time constants. This  
 428 assumption is also consistent with another derivation of the ocean-influence theory based on  
 429 Lagrangian path-integral<sup>25</sup>, where they assumed  $\lambda_L$  to be zero.

430 While the prior study focused on the horizontal advection from the ocean by assuming negligible  
 431  $E_L$ , we assume negligible horizontal advection. This assumption is justifiable in inland regions  
 432 where horizontal specific humidity differences are minimal (see Fig. 1). Mathematically, the  
 433 assumption of negligible horizontal advection can be expressed by considering  $l \rightarrow \infty$  in Eq. 8,  
 434 resulting in the following expression:

$$435 \quad q_L = \frac{1}{\rho v_2 (1 - \lambda_L)} E_L \quad (9)$$

436 or

$$437 \quad q_L = \beta E_L \quad (10)$$

438 where  $\beta = 1/\rho v_2 (1 - \lambda_L)$ , which depends primarily on the vertical mixing velocity at the top of  
 439 the ABL. At a climatically-relevant time scale and a global spatial scale,  $\beta$  could be considered  
 440 time constant because (1) changes in  $v_2$  can be damped by multiplication by  $1 - \lambda_L$ , and (2)

441 consistent changes in  $v_2$  across all land grid are unrealistic, although significant local-scale  
 442 changes in  $v_2$  could occur<sup>25</sup>. If we assume  $\beta$  as time constant,  $\beta$  can be understood as a partial  
 443 derivative of  $q_L$  with respect to  $E$ . The constant  $\beta$  in Eq. 10 also implies that the ratio of  $q_L$  and  $E_L$   
 444 remains approximately constant. Therefore, we can write as follows:

$$445 \quad \frac{\partial q_L}{\partial E_L} = \beta \quad (11)$$

446 and

$$447 \quad \frac{\Delta q_L}{q_L} = \frac{\Delta E_L}{E_L} \quad (12)$$

448 It is worth noting that Eq. 11 is conceptually similar to the sensitivity of the specific humidity to  
 449 changes in  $E$  introduced by McColl, et al.<sup>16</sup>. In their work, they also showed that  $\frac{\partial q_L}{\partial E}$  is largely  
 450 governed by the vertical mixing velocity at the top of ABL (i.e., the relaxation conductance in  
 451 their notation).

452 Eq. 12 leads to Eq. 2 in the main text.

### 453 **Application of the proposed equations to reanalysis and GCMs**

454 The proposed Eq. 3 was applied to each land grid cell. Specifically, we first calculated the  
 455 climatology of the multiplications of  $\Delta RH_L$  and  $\Delta T_L$  in Eq. 3 for each month and grid. For the  
 456 reanalysis applications presented in Fig. 3, the monthly climatology was multiplied by monthly  
 457 anomalies of  $RH_L$  and  $T_L$  at each grid cell. The resulting values for each grid cell and month were  
 458 spatially averaged with cosine-latitude weighting before computing annual average. In the case  
 459 of CMIP6 climate models depicted in Fig. 4, the monthly climatology was multiplied by  $\Delta RH_L$   
 460 and  $\Delta T_L$  representing the difference between the current (2003-2022) and past (1980-1999)  
 461 climate. Similar to the reanalysis dataset, the products were then spatially averaged using cosine-  
 462 latitude weighting.

463 The application of Eq. 5 paralleled that of Eq. 3, with the distinction that the ocean temperature  
 464 term ( $\Delta T_O$ ) needed to be incorporated.  $\Delta T_O$  was individually computed for each ocean grid cell  
 465 and subsequently spatially averaged using cosine-latitude weighting to derive the global average.  
 466 These global averaged  $\Delta T_O$  values were then introduced to each land grid cell for the application  
 467 of Eq. 5. The computation of other variables in Eq. 5 followed the same methodology as outlined  
 468 for Eq. 3.

469 In generating Fig. 6, which shows the application results of Eqs. 6 and 7, a challenge arose when  
 470 attempting to apply the equation to each grid cell. This challenge was rooted in the fact that the  
 471 first term on the right-hand side of Eq. 6 increases infinitely when  $E_L$  approaches zero. To  
 472 address this issue,  $\frac{RH_L}{E_L}$  was computed as the global mean of  $RH_L$  divided by the global mean of  
 473  $E_L$ . Subsequently, this global  $\frac{RH_L}{E_L}$  value was multiplied to Eq. 5 to derive Eq. 6, while other  
 474 variables were calculated at each grid cell and then spatially averaged by following the same  
 475 methodology as outlined in the above paragraph.



476

#### 477 **Data availability**

478 All data used in the main text and the supplementary information are publicly available. The  
479 FLUXNET2015 dataset can be obtained from the FLUXNET data portal  
480 (<https://fluxnet.org/data/fluxnet2015-dataset/>), the ERA5 reanalysis data can be obtained from  
481 CDS of ECMWF (<https://doi.org/10.24381/cds.f17050d7>), the JRA-3Q reanalysis data can be  
482 obtained from DIAS (<https://doi.org/10.20783/DIAS.645>), the CMIP6 models outputs can be  
483 obtained from CDS of the ECMWF (<https://doi.org/10.24381/cds.c866074c>).

484

#### 485 **Code availability**

486 The code used for these analyses will be publicly available prior to publication.

487

#### 488 **References**

- 489 1 Milly, P. C. D. *et al.* Stationarity Is Dead: Whither Water Management? *Science* **319**,  
490 573-574, (2008).
- 491 2 Jung, M. *et al.* Recent decline in the global land evapotranspiration trend due to limited  
492 moisture supply. *Nature* **467**, 951-954, (2010).
- 493 3 Fisher, J. B. *et al.* The future of evapotranspiration: Global requirements for ecosystem  
494 functioning, carbon and climate feedbacks, agricultural management, and water  
495 resources. *Water Resour. Res.* **53**, 2618-2626, (2017).
- 496 4 Milly, P. C. D. & Dunne, K. A. Colorado River flow dwindles as warming-driven loss of  
497 reflective snow energizes evaporation. *Science* **367**, 1252-1255, (2020).
- 498 5 Pan, S. *et al.* Evaluation of global terrestrial evapotranspiration using state-of-the-art  
499 approaches in remote sensing, machine learning and land surface modeling. *Hydrol.*  
500 *Earth Syst. Sci.* **24**, 1485-1509, (2020).
- 501 6 Yang, Y. *et al.* Evapotranspiration on a greening Earth. *Nat. Rev. Earth Environ.* **4**, 626-  
502 641, (2023).
- 503 7 Sherwood, S. & Fu, Q. A drier future? *Science* **343**, 737-739, (2014).
- 504 8 Vicente-Serrano, S. M., McVicar, T. R., Miralles, D. G., Yang, Y. & Tomas-Burguera,  
505 M. Unraveling the influence of atmospheric evaporative demand on drought and its  
506 response to climate change. *WIREs Clim. Chang.* **11**, e632, (2020).
- 507 9 McColl, K. A., Roderick, M. L., Berg, A. & Scheff, J. The terrestrial water cycle in a  
508 warming world. *Nat. Clim. Chang.* **12**, 604-606, (2022).
- 509 10 Scheff, J., Coats, S. & Laguë, M. M. Why do the Global Warming Responses of Land-  
510 Surface Models and Climatic Dryness Metrics Disagree? *Earth's Future* **10**,  
511 e2022EF002814, (2022).
- 512 11 Ault, T. R. On the essentials of drought in a changing climate. *Science* **368**, 256-260,  
513 (2020).
- 514 12 Wang, L. *et al.* Dryland productivity under a changing climate. *Nat. Clim. Chang.* **12**,  
515 981-994, (2022).
- 516 13 Zaitchik, B. F., Rodell, M., Biasutti, M. & Seneviratne, S. I. Wetting and drying trends  
517 under climate change. *Nat. Water.* **1**, 502-513, (2023).
- 518 14 Milly, P. C. D. & Dunne, K. A. Potential evapotranspiration and continental drying. *Nat.*  
519 *Clim. Chang.* **6**, 946-949, (2016).

520 15 Gentine, P., Chhang, A., Rigden, A. & Salvucci, G. Evaporation estimates using weather  
521 station data and boundary layer theory. *Geophys. Res. Lett.* **43**, 11,661-611,670, (2016).

522 16 McColl, K. A., Salvucci, G. D. & Gentine, P. Surface flux equilibrium theory explains an  
523 empirical estimate of water-limited daily evapotranspiration. *J. Adv. Model. Earth Syst.*  
524 **11**, 2036-2049, (2019).

525 17 Kim, Y. *et al.* Relative humidity gradients as a key constraint on terrestrial water and  
526 energy fluxes. *Hydrol. Earth Syst. Sci.* **25**, 5175-5191, (2021).

527 18 Vargas Zeppetello, L. R. *et al.* Apparent surface conductance sensitivity to vapour  
528 pressure deficit in the absence of plants. *Nat. Water.* **1**, 941-951, (2023).

529 19 Kim, Y., Garcia, M., Black, T. A. & Johnson, M. Assessing the complementary role of  
530 surface flux equilibrium (SFE) theory and maximum entropy production (MEP) principle  
531 in the estimation of actual evapotranspiration. *J. Adv. Model. Earth Syst.* **15**, (2023).

532 20 McColl, K. A. & Tang, L. I. An Analytic Theory of Near-Surface Relative Humidity over  
533 Land. *J. Clim.* **37**, 1213-1230, (2024).

534 21 Ma, H.-Y. *et al.* CAUSES: On the Role of Surface Energy Budget Errors to the Warm  
535 Surface Air Temperature Error Over the Central United States. *J. Geophys. Res. Atmos.*  
536 **123**, 2888-2909, (2018).

537 22 Dong, J., Lei, F. & Crow, W. T. Land transpiration-evaporation partitioning errors  
538 responsible for modeled summertime warm bias in the central United States. *Nat.*  
539 *Commun* **13**, 336, (2022).

540 23 Willett, K. *et al.* HadISDH land surface multi-variable humidity and temperature record  
541 for climate monitoring. *Clim. Past* **10**, 1983–2006, (2014).

542 24 Simmons, A. J., Willett, K. M., Jones, P. D., Thorne, P. W. & Dee, D. P. Low-frequency  
543 variations in surface atmospheric humidity, temperature, and precipitation: Inferences  
544 from reanalyses and monthly gridded observational data sets. *J. Geophys. Res. Atmos.*  
545 **115**, (2010).

546 25 Chadwick, R., Good, P. & Willett, K. A Simple Moisture Advection Model of Specific  
547 Humidity Change over Land in Response to SST Warming. *J. Clim.* **29**, 7613-7632,  
548 (2016).

549 26 Byrne, M. P. & O’Gorman, P. A. Understanding decreases in land relative humidity with  
550 global warming: conceptual model and GCM simulations. *J. Clim.* **29**, 9045-9061,  
551 (2016).

552 27 Byrne, M. P. & O’Gorman, P. A. Trends in continental temperature and humidity directly  
553 linked to ocean warming. *Proc. Nat. Acad. Sci. U.S.A.* **115**, 4863-4868, (2018).

554 28 Berg, A. & Sheffield, J. Climate change and drought: the soil moisture perspective. *Curr.*  
555 *Clim. Change Rep.* **4**, 180-191, (2018).

556 29 Kim, Y., Garcia, M. & Johnson, M. Land-atmosphere coupling constrains increases to  
557 potential evaporation in a warming climate: Implications at local and global scales.  
558 *Earth's Future* **11**, e2022EF002886, (2023).

559 30 Vicente-Serrano, S. M. *et al.* Recent changes of relative humidity: regional connections  
560 with land and ocean processes. *Earth Syst. Dynam.* **9**, 915-937, (2018).

561 31 Berg, A. *et al.* Land–atmosphere feedbacks amplify aridity increase over land under  
562 global warming. *Nat. Clim. Chang.* **6**, 869-874, (2016).

563 32 Zhou, W., Leung, L. R. & Lu, J. The Role of Interactive Soil Moisture in Land Drying  
564 Under Anthropogenic Warming. *Geophys. Res. Lett.* **50**, e2023GL105308, (2023).

565 33 Douville, H. & Plazzotta, M. Midlatitude Summer Drying: An Underestimated Threat in  
566 CMIP5 Models? *Geophys. Res. Lett.* **44**, 9967-9975, (2017).

567 34 Dunn, R. J. H., Willett, K. M., Ciavarella, A. & Stott, P. A. Comparison of land surface  
568 humidity between observations and CMIP5 models. *Earth Syst. Dynam.* **8**, 719-747,  
569 (2017).

570 35 Simpson, I. R. *et al.* Observed humidity trends in dry regions contradict climate models.  
571 *Proc. Nat. Acad. Sci. U.S.A.* **121**, e2302480120, (2024).

572 36 Allan, R. P. *et al.* Advances in understanding large-scale responses of the water cycle to  
573 climate change. *Ann. N.Y. Acad. Sci.* **1472**, 49-75, (2020).

574 37 Douville, H. & Willett, K. M. A drier than expected future, supported by near-surface  
575 relative humidity observations. *Sci. Adv.* **9**, eade6253, (2023).

576 38 Pastorello, G. *et al.* The FLUXNET2015 dataset and the ONEFlux processing pipeline  
577 for eddy covariance data. *Sci. Data* **7**, 225, (2020).

578 39 Hersbach, H. *et al.* The ERA5 global reanalysis. *Q. J. Roy. Meteorol. Soc.* **146**, 1999-  
579 2049, (2020).

580 40 Kosaka, Y. *et al.* The JRA-3Q Reanalysis. *Journal of the Meteorological Society of*  
581 *Japan. Ser. II* **102**, 49-109, (2024).

582 41 Eyring, V. *et al.* Overview of the Coupled Model Intercomparison Project Phase 6  
583 (CMIP6) experimental design and organization. *Geosci. Model Dev* **9**, 1937-1958,  
584 (2016).

585 42 McColl, K. A. & Rigden, A. J. Emergent Simplicity of Continental Evapotranspiration.  
586 *Geophys. Res. Lett.* **47**, e2020GL087101, (2020).

587 43 Chen, S., McColl, K. A., Berg, A. & Huang, Y. Surface Flux Equilibrium Estimates of  
588 Evapotranspiration at Large Spatial Scales. *J. Hydrometeorol.* **22**, 765-779, (2021).

589 44 Seltzer, A. M., Blard, P.-H., Sherwood, S. C. & Kageyama, M. Terrestrial amplification  
590 of past, present, and future climate change. *Sci. Adv.* **9**, eadf8119, (2023).

591 45 O’Gorman, P. A. & Muller, C. J. How closely do changes in surface and column water  
592 vapor follow Clausius–Clapeyron scaling in climate change simulations? *Environ. Res.*  
593 *Lett.* **5**, 025207, (2010).

594 46 Held, I. M. & Soden, B. J. Robust responses of the hydrological cycle to global warming.  
595 *J. Clim.* **19**, 5686-5699, (2006).

596 47 Douville, H. *et al.* Drivers of the enhanced decline of land near-surface relative humidity  
597 to abrupt 4xCO<sub>2</sub> in CNRM-CM6-1. *Clim. Dyn.* **55**, 1613-1629, (2020).

598 48 Byrne, M. P. Amplified warming of extreme temperatures over tropical land. *Nat.*  
599 *Geosci.* **14**, 837-841, (2021).

600 49 Allan, R. P., Willett, K. M., John, V. O. & Trent, T. Global Changes in Water Vapor  
601 1979–2020. *J. Geophys. Res. Atmos.* **127**, e2022JD036728, (2022).

602 50 Xu, W. *et al.* Weakened Increase in Global Near-Surface Water Vapor Pressure During  
603 the Last 20 Years. *Geophys. Res. Lett.* **51**, e2023GL107909, (2024).

604 51 Ma, N., Zhang, Y. & Szilagyi, J. Water-balance-based evapotranspiration for 56 large  
605 river basins: A benchmarking dataset for global terrestrial evapotranspiration modeling.  
606 *J. Hydrol.*, 130607, (2024).

607 52 Knauer, J., El-Madany, T. S., Zaehle, S. & Migliavacca, M. Bigleaf—An R package for  
608 the calculation of physical and physiological ecosystem properties from eddy covariance  
609 data. *PLOS ONE* **13**, e0201114, (2018).

610 53 Twine, T. E. *et al.* Correcting eddy-covariance flux underestimates over a grassland. *Agr.*  
611 *Forest Meteorol.* **103**, 279-300, (2000).  
612

613  
614 **Acknowledgments**

615 We acknowledge the support of the Canadian Space Agency (CSA) Grant 21SUESIELH. We are  
616 grateful for FLUXNET2015 site PIs, ERA5 and JRA-3Q reanalysis developing groups, and the  
617 CMIP6 climate modelling groups, and appreciate the efforts of data providers for producing and  
618 making available these datasets. We express our thanks to the development of the ocean-  
619 influence theory (by M. Byrne, P. O’Gorman, R. Chadwick, P. Good, K. Willett, and others) that  
620 inspired our theoretical framework.

621  
622 **Author contributions**

623 Conceptualization: YK, MSJ

624 Methodology: YK, MSJ

625 Investigation: YK, MSJ

626 Visualization: YK

627 Supervision: MSJ

628 Writing—original draft: YK

629 Writing—review & editing: MSJ

630

631 **Competing interests**

632 Authors declare that they have no competing interests.

633

634 **Supplementary Information**

635 Supplementary Information file includes:

636 Figs. S1 to S2

637 Tables S1